Assessment of Buffet Forcing Function Development Process Using Unsteady Pressure Sensitive Paint

Martin K. Sekula,[1] David J. Piatak,[2] and Russ D. Rausch[3]

NASA Langley Research Center, Hampton, VA, 23681, USA

James C. Ross[4]

NASA Ames Research Center, Moffett Field, CA, 94035, USA

and

Marvin E. Sellers[5]

QuantiTech, Arnold AFB, TN, 37389, USA

A wind tunnel test was conducted at the Ames Unitary Plan Wind Tunnel to characterize the transonic buffet environment of a generic launch vehicle forebody. The test examined a highly instrumented version of the Coe and Nute Model 11 test article first tested in the 1960s. One of the measurement techniques used during this test was unsteady pressure sensitive paint (uPSP) developed at the Arnold Engineering Development Complex. This optical measurement technique measured fluctuating pressures at over 300,000 locations on the surface of the model. The high spatial density of these measurements provided an opportunity to examine in depth the assumptions underpinning the development of buffet forcing functions (BFFs) used in the development of the Space Launch System vehicle. The comparison of discrete-measurement-based BFFs to BFFs developed by continuous surface pressure integration indicates that the current BFF development approach underpredicts low-frequency content of the BFFs while overpredicting high frequency content. Coherence-based adjustments employed to reduce overprediction in the surface integration of discrete pressure measurements contribute to the inaccuracy of the BFFs and their implementation should be reevaluated.

I.   Introduction

Transonic buffet is one of the most severe aerodynamic phenomena that a rocket experiences during launch. As a launch vehicle approaches the transonic regime, Mach 0.8 to 1.2, large amplitude pressure fluctuations are produced by phenomena such as flow separation and shock dynamics. The unsteady aerodynamic forces produced by these phenomena can excite both global and local vehicle structural response. The consequences of incorporating poorly characterized buffet forces into the design process can range from inefficient structures that can reduce the vehicle capabilities to undersized structures that, in the worst case scenario, may result in structural failure (Refs. 1, 2, 3). It is thus imperative to appropriately characterize the transonic buffet environment.

Modeling buffet-related aerodynamic forces is accomplished by developing buffet forcing functions (BFFs) – a series of orthogonal force time histories acting at various longitudinal stations on the vehicle centerline, each representing the net forces caused by surface pressures acting on a longitudinal segment of the vehicle. Buffet forcing functions are traditionally developed using experimentally-measured pressure time histories that are acquired using a rigid wind

---

[1] Research Aerospace Engineer, Aeroelasticity Branch, and Senior Member AIAA.
[2] Research Aerospace Engineer, Aeroelasticity Branch, and Senior Member AIAA.
[3] Assistant Branch Head, Aeroelasticity Branch, and Associate Fellow AIAA.
[4] Senior Aerospace Engineer, Experimental Aero-Physics Branch, and Associate Fellow AIAA.
[5] AEDC Fellow, Integrated Test & Evaluation, Flight Systems, 740 Fourth St. MS6001.

tunnel model of a launch vehicle tested at transonic conditions. Analytical forcing functions based on time-accurate Computational Fluid Dynamics (CFD) methods are currently not practical due to prohibitively computationally-expensive solutions (Ref. 4), but have been used to provide additional insight into the buffet environment for specific problems (Ref. 4, 5). On the other hand, steady-state CFD solutions are used extensively to help determine sensor placement on rigid buffet models since proper sensor placement is critical in BFF development. In addition to these CFD solutions, the distribution of sensors on the surface of these models is based on a combination of other factors including the model outer mold line (OML), data acquisition system/facility limitations, model volume, engineering judgement, and budget. Satisfying all these conflicting needs and restrictions results in a sparsely-instrumented model of a launch vehicle.

The most-instrumented transonic buffet model tested by NASA incorporated only 472 unsteady pressure sensors in its design (Ref. 6). Measurements from some of these sensors were used to approximate the fluctuating surface pressures acting on a patch of the full-scale vehicle with a wetted surface area as large as 270 square feet (Ref. 7). Accurate extrapolation of pressure variation between such widely-spaced sensors is not possible and the current approach of applying the measured pressure time history to the entire surface area causes a significant overprediction of the resulting fluctuating force. The SLS project team adjusts these forces using coherence-based factors that reduce the effective surface area used in the pressure integration, thereby approximating the effects of temporal and spatial variation in surface pressure (Ref. 7).

In 2015, a wind tunnel test – called the Buffet Verification Test (BVT) – was conducted at the Ames Unitary Plan Wind Tunnel, 11-foot test section (Ref. 8). The test used a highly instrumented copy of a previously-tested notional launch vehicle forebody as a platform to develop new measurement techniques and improve the understanding of the transonic buffet environment. This model, based on the Model 11 tested by Coe and Nute (Ref. 9), is a simple axisymmetric launch vehicle geometry, where a large payload fairing is attached to a smaller-diameter second stage. This configuration is found on many modern launch vehicles and is conducive to producing a highly-unsteady buffet environment (Ref. 1). The instrumentation suite employed in the BVT included static pressure taps, unsteady pressure transducers, accelerometers, four-component balance, shadowgraph and infrared imaging, and unsteady pressure sensitive paint (uPSP). Unsteady PSP had previously been demonstrated (Ref. 10) in the large wind tunnel at AEDC and was requested to partner with NASA to provide uPSP data for this test. The advent of uPSP has provided an opportunity to examine in depth the assumptions underpinning the development of BFFs, such as the coherence factors. This work examines some of the assumptions and approximations currently used in the development of BFFs by comparing these estimates with those generated by direct integration of extremely dense uPSP measurements.

II. Buffet Forcing Function Development Methodology

The current state-of-the-art BFF development method is based on discrete, unsteady pressure measurements acquired using pressure transducers embedded in the skin of a rigid wind tunnel model. The general outline of this multistep process is presented in Figure 1. A detailed discussion of the BFF development method can be found in References 7 and 10. The sparse distribution of sensors requires that discrete pressure measurements are integrated over large surface areas and then adjusted using coherence-based factors to account for spatially and temporally varying pressure unsteadiness across the integration surface.

The BFF development process significantly relies on engineering judgement. Among the choices made by engineers are: location of sensors, integration boundaries, frequency range used for the coherence analysis, and selection of longitudinal aerodynamic regions (i.e., defining vehicle regions dominated by a single unsteady aerodynamic phenomenon). Each of these decisions can have an impact on the final BFFs. Using uPSP measurements circumvents the majority of these somewhat subjective decisions by acquiring continuous surface pressure measurements, thereby replacing all the steps within the red dash-line box in the BFF development diagram (Figure 1) with a simple surface integration without the aforementioned engineering assumptions.

A. Unsteady Pressure Sensitive Paint Data

Equipment and data processing methodologies from AEDC were used to produce the uPSP time history data and details of this process can be found in Ref. 11. The uPSP data were mapped to a model surface grid, providing unsteady surface pressure data at almost 305,000 locations on the surface of the model, as shown in Figure 2. The grid consists of rings of measurement locations at approximately 700 longitudinal stations down the length of the model. Each ring is made up of between 260 to 1200 discrete measurement locations. Due to the scale of the aerodynamic phenomena being measured and the spatial density of the measurement grid, the uPSP data approximates

a continuous surface pressure measurement. Each uPSP data record consists of 10-second time histories of fluctuating pressures at each grid point acquired at a sample rate of 5000 Hz.
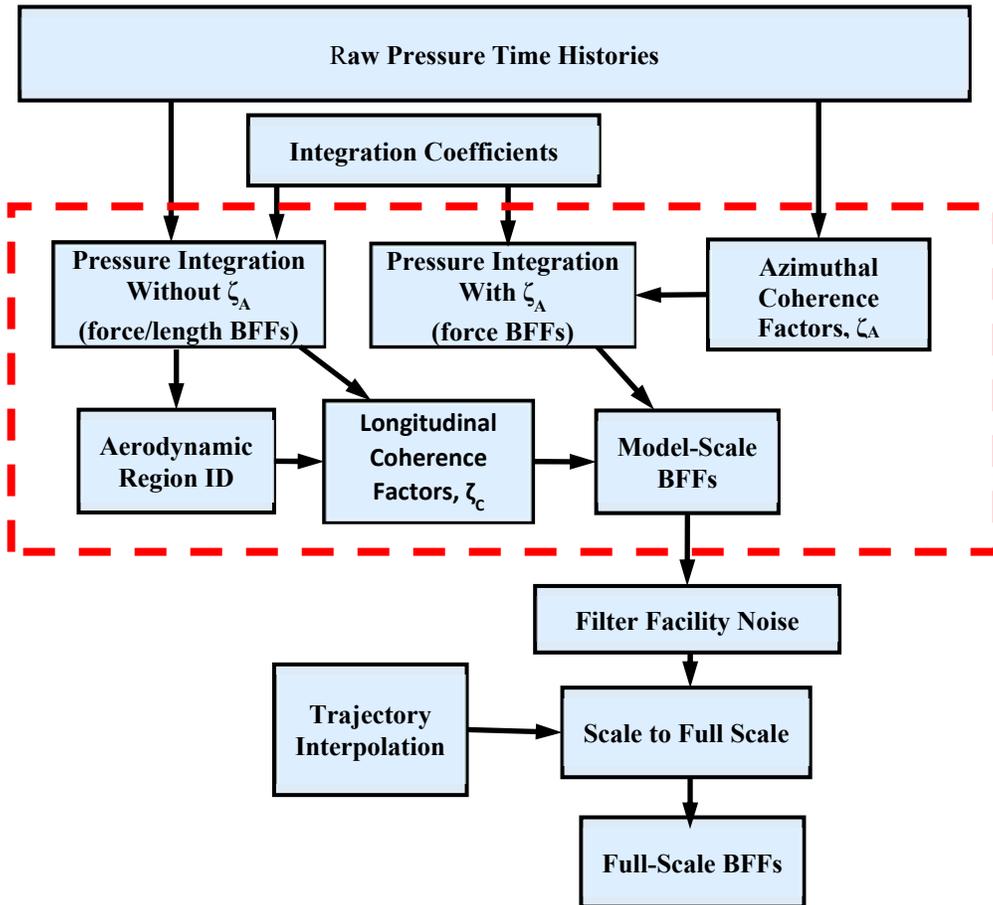

Figure 1. Flow diagram of buffet forcing function development process. (Blocks contained in red dashed box can be eliminated when continuous surface pressure measurements from uPSP are used.)
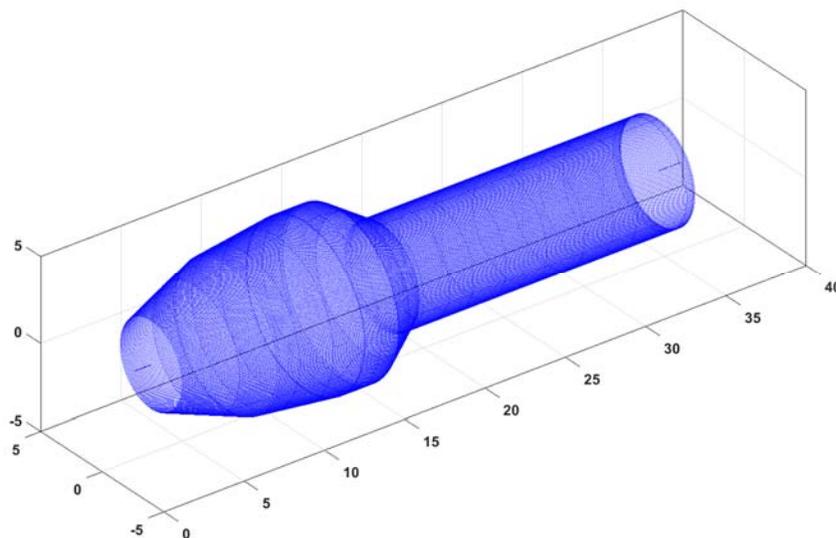

Figure 2. 3-D representation of a sample uPSP grid.

B. Surface Integration

The choice of integration areas for discrete pressure measurements is based on the combination of major OML changes, such as cone-cylinder junctions, and halfway points (both longitudinal and circumferential) between adjacent sensors. The physical sensor locations on the BVT model and the associated integration areas for the sensors are presented in Figure 3. The locations of the transducers are depicted by black points and the integration boundaries for the transducers are represented by red and green lines.
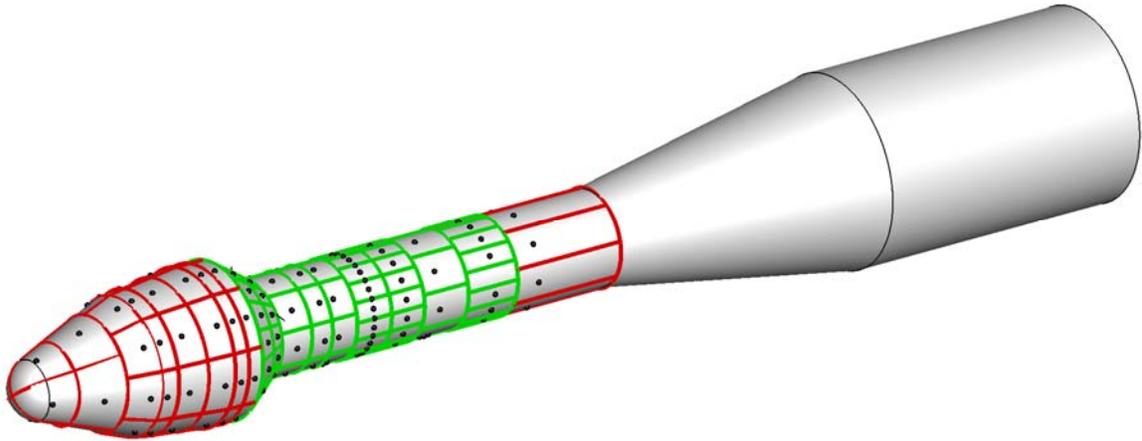

Figure 3. BVT model sensor locations and integration boundaries. (The region examined in this study is represented by the green integration boundaries.)

C. Pressure Sensor– uPSP Comparison

Traditional pressure transducers (PTs) embedded in the model skin are simulated using uPSP measurements by identifying the closest location on the uPSP surface grid to each PT. These grid locations, or virtual pressure transducers (vPTs), are then used to provide a direct comparison between BFFs developed using the current state-of-the-art techniques that use discrete pressure measurements and coherence-based integration adjustments.

A sample comparison of the BFF standard deviation (root-mean-square with mean removed, but for simplicity referred to as *rms* henceforth) is presented in Figure 4. The blue circles represent PT-based BFF data while the red squares represent the vPT-based BFF data. The BFF data are plotted as a function of longitudinal station and is separated into longitudinal (F_x), lateral (F_y), and vertical (F_z) components. The aftmost ring of sensors in Figure 3 is not used in this comparison, since the uPSP data did not entirely cover this segment of the model. In general, Figure 4 indicates that the level of unsteadiness in the PT- and vPT-based BFFs is similar and the overall trends for all three components of the BFFs match well.

Although the BFF rms levels appear to indicate that the uPSP measurements match the physical sensor measurements well, examining the coherence data for the two data sets indicates otherwise. The coherence lengths as a function of longitudinal station are presented in Figure 5a and the coherence angles as a function of longitudinal station are presented in Figure 5b. The PT-derived coherence parameters are presented in blue and the vPT-derived coherence parameters are presented in red. The data indicates that forward of the frustum (approx. station 15 inches) the trends and magnitude of the coherence do not match for the PT and vPT data, therefore, the frequency content of the uPSP measurements on the forebody may not be properly resolved. This problem may be due to poor signal-to-noise ratio and small magnitude pressure fluctuations in that region (Ref. 8). These differences in the coherence lengths and angles were noted for the entire range of Mach numbers and model attitudes examined. As a consequence, only the uPSP data located within the boundaries highlighted in green in Figure 3, will be considered in this analysis.
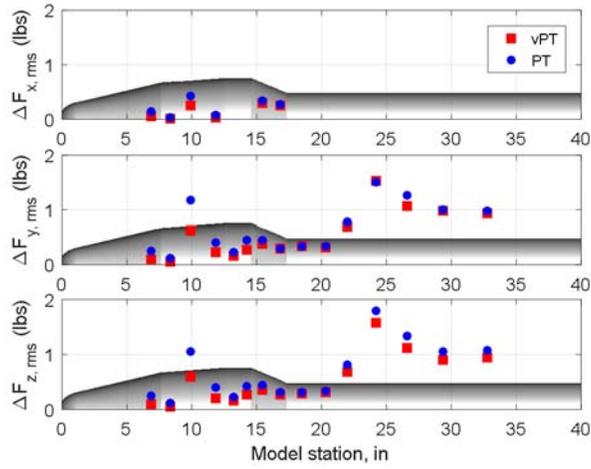
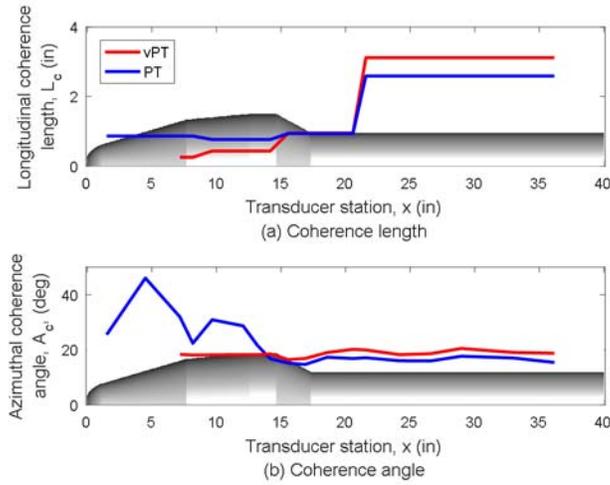**Figure 4. Sample comparison of BFF ΔF_{rms} based on PT and vPT, M=0.92, α=0°.**

Figure 5. Sample comparison of coherence lengths and angles based on PT and vPT, M=0.92, α=0°.

III. Continuous Integration vs. vPT-based BFFs

In order to understand how the various assumptions in the BFF development process (outlined in Figure 1) impact the fidelity of the BFFs, forcing functions were generated using uPSP-derived discrete measurements (vPTs) and compared to forcing functions developed by integrating the continuous uPSP over the same longitudinal segments of the model. vPT-based BFFs were developed using various vPT distributions selected to isolate the impact of a few key BFF-development assumptions and wind tunnel model design choices. These variations included azimuthal density of sensors, longitudinal density of sensors, and longitudinal location of sensors within an integration area.

As described in the previous section, the uPSP data used in this analysis are limited to the aft half of the BVT model, downstream of station 14.7 inches. Likewise, the aftmost instrumented segment of the model, downstream of station 34.6 inches, lacked complete uPSP surface coverage and is not included in this analysis. The surface region of the model examined in this study is highlighted in green in Figure 3. This study includes 28 wind tunnel data points at a range of Mach numbers, model angle of attack, and Reynolds numbers provided in Table 1. Note that uPSP data were not available for all combinations of listed test conditions, hence only 28 out of 30 combinations are utilized.

The BFFs are analyzed using several approaches including a comparison of standard deviation (rms), power spectral density functions (PSDs), and cross-PSDs. Throughout this paper, the PSDs, cross-PSDs, and coherence functions

were computed with a 2^{12} window size, 2^{12} discrete Fourier transform points, 50% window length overlap, and a Hamming window was applied to reduce spectral leakage.

The large number of BFFs in this data set – 560 BFFs (20 BFF components x 28 data points) – makes it impractical to examine all the data individually. Therefore, along with some sample comparisons, extensive use of histograms and other statistical techniques is required to understand the overall trends in the data.

Table 1. Test conditions.

Mach	0.80, 0.85, 0.92, 1.025, 1.10
Angle of attack (deg)	-4, 0, 4
Reynolds number (ft^{-1})	3e6, 5e6

A. Effect of Azimuthal Sensor Density

One of the choices required in the design of a wind tunnel model is the azimuthal sensor density, or the number of sensors located at a particular model station. These sensors are usually distributed in an axisymmetric manner around the circumference of the model.

1. Trends in Overall BFF Fluctuation

Histograms are used to understand the trends in how the azimuthal density of sensors affects the overall fluctuation of BFFs. The histograms were created by calculating the rms levels of vPT-based BFFs and comparing them to BFFs developed by performing a continuous surface integration of the uPSP data over the same segments of the model. A percent error in rms values relative to the continuous integration BFFs was determined for BFFs developed using 4, 8, 16, and 32 vPTs per ring of sensors. A negative error implies that the BFFs from discrete (virtual) pressure measurements are underpredicting the overall fluctuations. These histograms only include the BFFs for the integration segments on the frustum and aft of the frustum.

Histograms of the rms error for BFFs developed using 4, 8, 16, and 32 vPTs are provided in Figures 6 through 9, respectively. The data used to develop the histograms were parsed in two ways in order to provide some further insight about the accuracy of the BFF development methodology. First, the BFF data were divided into two cases: 0 degree angle of attack and 4 degree angle of attack (provided in subfigures *a* and *b* in Figures 6 through 9; the combined dataset is presented in subfigure *c*). The data were also separated into the three orthogonal components of the BFFs: longitudinal, lateral, and vertical.

The first notable characteristic of all the histograms in Figures 6 through 9 is the non-Gaussian, two-peak distribution. The underlying cause of this distribution is that the BFFs used in this study are dominated by two distinct aerodynamic phenomena – the separated flow aft of the frustum and the reattached flow further downstream on the model. Separating the BFFs by regions dominated by each aerodynamic phenomenon results in a Gaussian histogram distribution for each subset of data (not presented). The histograms produced by these two subsets of BFFs are separated by an offset in the percent error: the separated flow (SF) region exhibits a larger percent error (more to the left on the abscissa) in underpredicting the overall fluctuations than the reattached flow (RF) region (more to the right on the abscissa). To highlight this difference in the BFFs for the two aerodynamic regions in Figures 6 through 9, the components of the histograms that represent the RF region data are outlined with a thicker border. These differing offsets indicate that the current approach used to generate BFFs varies in its ability to model the overall fluctuations of the buffet loads due to different aerodynamic phenomena.

The second observation about the histograms is that comparing the zero and four degree angle-of-attack cases, the change in histogram distribution is minimal, indicating that the level accuracy of the BFF development approach is not affected by changes in angle of attack. Furthermore, the axisymmetric nature of the model implies that there should be no difference in the histograms of the vertical and lateral BFF components at zero degree angle of attack, Figures 6a through 9a. This observation also holds true for the four degree angle of attack, see Figures 6b through 9b. An explanation for this angle-of-attack insensitivity is yet to be determined.

The last observation, based on Figures 6 through 9, is that the number of sensors used to develop the BFFs affects how well the actual aerodynamic forces are modeled. As the number of sensors increases from 4 to 32, the histograms shift in the positive direction – an indication that lower circumferential sensor density results in lower overall fluctuation in the resulting BFFs. This observation is further substantiated and quantified by the median value and

percentage of underpredicted cases provided in Table 2. It should also be noted that the peak associated with the reattached flow region shifts entirely to the positive side of the abscissa for the 16-sensors per ring cases, Figure 8. Increasing the number of sensors per ring to 32 shifts the histogram even further such that the peak associated with the separated flow region is centered on the abscissa origin.

The mean, median, standard deviation and percentage of BFFs that are underpredicted, corresponding to the histograms in Figures 6 through 9, are provided in Tables 2(a-c). The tables group the data by the number of sensors per ring used to develop the BFFs, subdivide the data by region, and by the direction of the BFF component (longitudinal, lateral, and vertical). The data were not separated by angle of attack since it was shown to have minimal impact on the histogram trends. The tables quantify the trends identified in the histograms. In addition, the table data indicates that the standard deviation for the RF region are larger than the standard deviation for the SF region. This observation implies that the current BFF development process is less consistent in modeling the BFFs unsteady aerodynamic forces in the RF region than the SF region. It should also be noted that the number of sensors per ring does not affect the standard deviation of the histogram for either region, only the mean values of the percent difference.
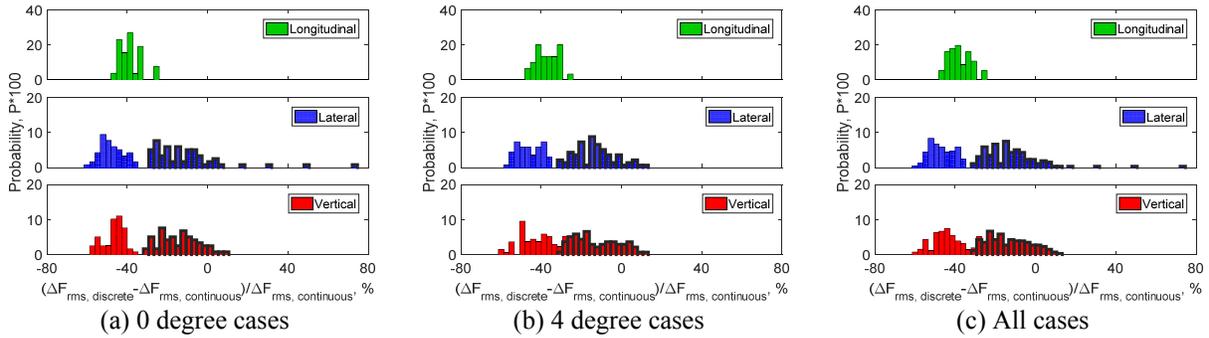

(a) 0 degree cases   (b) 4 degree cases   (c) All cases

Figure 6. Histogram of percent difference in BFF ΔF_{rms} based on continuous integration and 4 vPTs/ring.

(a) 0 degree cases   (b) 4 degree cases   (c) All cases
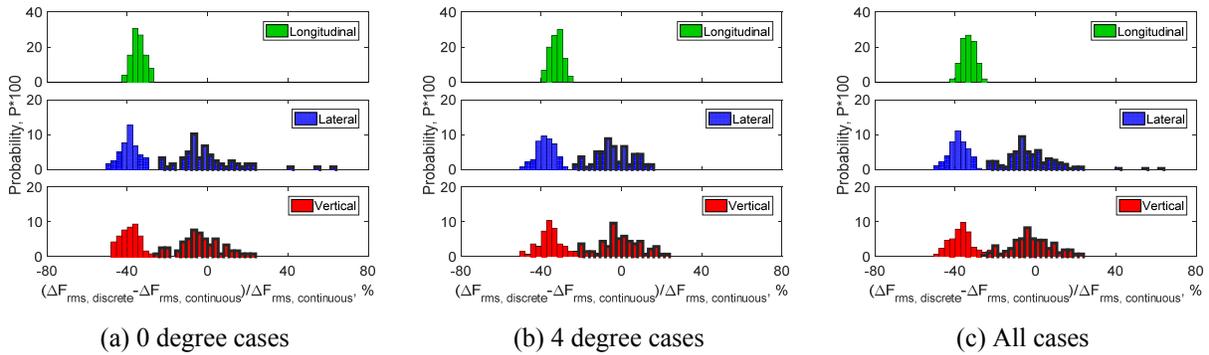
Figure 7. Histogram of percent difference in BFF ΔF_{rms} based on continuous integration and 8 vPTs/ring.

(a) 0 degree cases   (b) 4 degree cases   (c) All cases
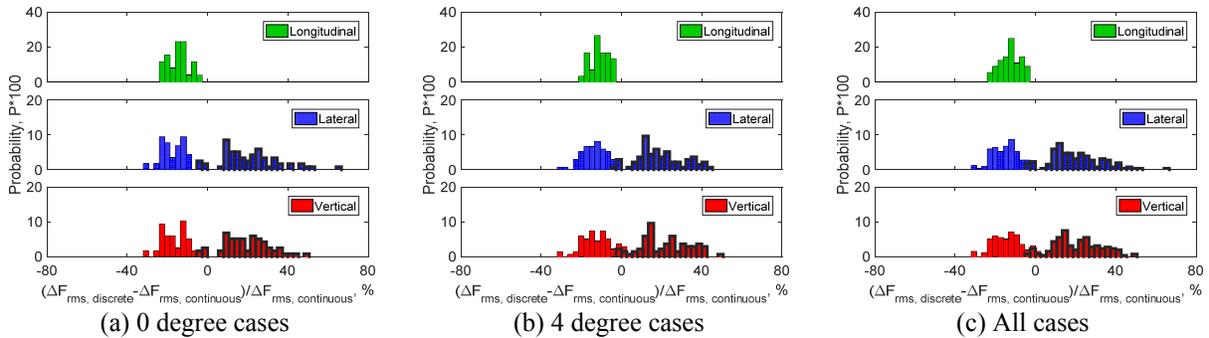
Figure 8. Histogram of percent difference in BFF ΔF_{rms} based on continuous integration and 16 vPTs/ring.

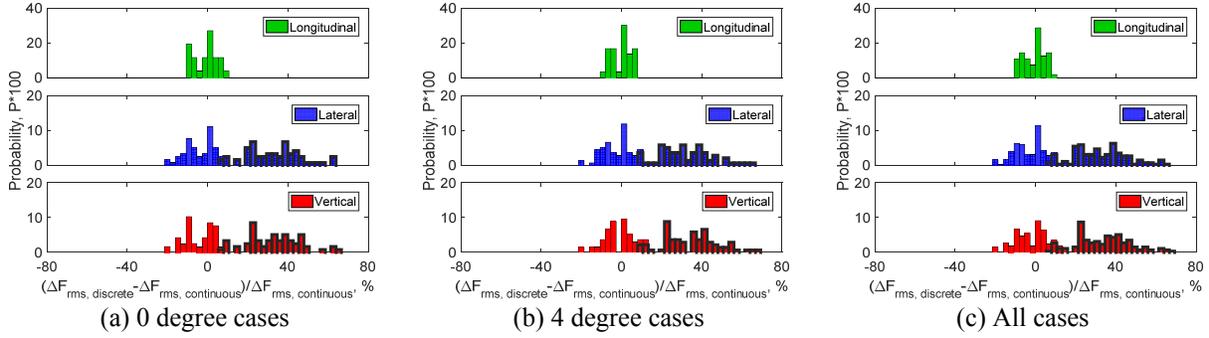(a) 0 degree cases   (b) 4 degree cases   (c) All cases

Figure 9. Histogram of percent difference in BFF ΔF$_{rms}$ based on continuous integration and 32 vPTs/ring.

Table 2a. Statistical values percent difference in BFF ΔF$_{x, rms}$ (longitudinal) based on continuous integration and vPTs.

		4 sensor	8 sensor	16 sensor	32 sensor
Mean	SF Region	-37.7	-33.4	-12.6	-0.4
	RF Region	n/a	n/a	n/a	n/a
	Both Regions	-37.7	-33.4	-12.6	-0.4
Median	SF Region	-38.7	-33.2	-12.1	1.0
	RF Region	n/a	n/a	n/a	n/a
	Both Regions	-38.7	-33.2	-12.1	1.0
Standard deviation	SF Region	5.4	3.4	5.1	5.4
	RF Region	n/a	n/a	n/a	n/a
	Both Regions	5.4	3.4	5.1	5.4
% under-prediction	SF Region	100	100	100	42.9
	RF Region	n/a	n/a	n/a	n/a
	Both Regions	100	100	100	42.9

Table 2b. Statistical values percent difference in BFF ΔF$_{y, rms}$ (lateral) based on continuous integration and vPTs.

		4 sensor	8 sensor	16 sensor	32 sensor
Mean	SF Region	-46.7	-38.4	-15.7	-4.0
	RF Region	-11.5	-2.0	20.2	32.5
	Both Regions	-27.1	-18.2	4.2	16.3
Median	SF Region	-47.1	-38.2	-14.7	-3.9
	RF Region	-13.8	-4.4	18.4	31.4
	Both Regions	-26.0	-17.5	7.6	16.6
Standard deviation	SF Region	5.9	4.8	5.8	6.9
	RF Region	16.1	13.0	12.7	13.3
	Both Regions	21.6	20.8	20.6	21.2
% under-prediction	SF Region	100	100	100	58.9
	RF Region	86.4	63.6	7.1	0
	Both Regions	92.5	79.8	48.4	26.2

8

Table 2c. Statistical values percent difference in BFF $\Delta F_{z, rms}$ (vertical) based on continuous integration and vPTs.

		4 sensor	8 sensor	16 sensor	32 sensor
Mean	SF Region	-45.0	-37.2	-15.0	-3.3
	RF Region	-13.2	-1.8	20.7	33.8
	Both Regions	-27.3	-17.6	4.9	17.3
Median	SF Region	-45.0	-37.1	-14.5	-3.6
	RF Region	-15.0	-2.6	19.8	34.4
	Both Regions	-26.6	-16.5	7.0	17.3
Standard deviation	SF Region	7.0	5.3	6.7	7.3
	RF Region	10.6	10.5	11.8	13.5
	Both Regions	18.3	19.6	20.3	21.6
% under-prediction	SF Region	100	100	98.2	57.1
	RF Region	85.7	59.3	5.7	0
	Both Regions	92.1	77.4	46.8	25.4

2. In-Depth Analysis

In order to better understand the trends identified above, it is useful to examine a single test condition in more detail. The condition chosen for this study is Mach 0.92, angle of attack of 0 degrees – a flight condition typically associated with large buffet-related aerodynamic fluctuations (Ref. 1, 7, 10). The impact of azimuthal density of sensors on overall fluctuation of BFFs for this test condition is presented in Figure 10, where four circumferential sensor densities in each ring of sensors are shown (4, 8, 16, and 32 vPTs per ring). The rms values of the various BFFs are compared to the continuous uPSP-based BFFs. There are three interesting trends to note: 1) As the number of sensors is increased azimuthally, the rms level of the BFFs increases; 2) On the frustum and within the separated flow region created by the frustum, the rms levels are underpredicted by the discrete measurement-based BFFs and as the azimuthal sensor density increases, it approaches the continuous integration BFF rms levels; and 3) Aft of the separated flow region (>24 inches) the low sensor density BFFs resulted in rms levels on par with the continuous integration. Increasing the sensor density resulted in the overprediction of rms levels. These observations mirror the ones noted for histograms in Figures 6 through 9.

There are three elements in the BFF development process (Figure 1) that can affect the magnitude of BFF unsteadiness: coherence angles, coherence lengths, and unsteadiness changes directly related to the number of sensors used in the integration process. The effect of the number of sensors on each of these parameters is presented in Figures 11 through 16.

The effect of azimuthal sensor density on azimuthal coherence angles is presented in Figure 11a. Coherence angles tend to decrease with increasing sensor density. The cause of this dependence can be identified by examining the effect of sensor density on the exponential curve fit employed to identify the angle at which the magnitude-squared coherence is equal to 50 percent, more commonly referred to as the coherence angle.

Figure 12 demonstrates the impact of sensor density on these curve fits. The separation angle between sensors used in the coherence calculation is provided on the abscissa. The ordinate represents the mean of the coherence function calculated for 0.5 to 800 Hz. The colors indicate the number of sensors used in calculating the force-per-length BFFs used in the coherence calculation, and identifies the coherence data used in the calculation of the curve fit. The four-sensor rings (red) have a minimum separation angle of 90 degrees. Increasing the number of sensors in the rings reduces the minimum separation angle, which shifts the curve fit to the left, resulting in an improved approximation of the exponential decay compared to the experimental data. The exponential curve fit in Figure 12 is a poor approximation of the azimuthal coherence decay, even though it is weighted towards the shorter separation angles (Ref. 7).

During the BFF development process, two longitudinal regions dominated by distinct aerodynamic phenomena were identified. Based on the longitudinal integration boundaries, these aerodynamic regions encompassed model segments from 14.70 to 21.10 inches (separated flow region) and 21.10 to 34.60 inches (reattached flow region) – regions previously noted in the discussion of Figures 6 through 9. The effect of azimuthal sensor density on the longitudinal coherence lengths within these two aerodynamic regions is presented in Figure 11b. Within both regions, the

coherence lengths increase if the azimuthal sensor density is increased. Unlike the coherence angles, where an increase in the number of sensors per ring reduced the separation distance between sensors, the separation distance between the rings of sensors does not change, as is noted by the fixed separation distances in Figure 13 – the impact of azimuthal sensor density on longitudinal coherence and exponential fit of its decay. The trends noted in Figure 13 indicate that the change in longitudinal coherence is purely a function of BFF frequency content and how it is affected by the number of sensors in each ring.

The effect of sensor density on coherence is presented in Figures 14 and 15. Longitudinal coherence functions for sectional BFFs calculated between stations 15.57 and 16.87 inches (located in the SF Region) are presented in Figure 14 and coherence functions for sectional BFFs calculated between stations 28.97 and 33.00 inches (located in the RF Region) are presented in Figure 15. Within both aerodynamic regions, coherence functions based on 4-sensor BFFs (red line) significantly underpredict the coherence compared to BFFs developed based on continuous circumferential integration (black). Increasing the number of sensore from 4 to 8 (maroon line) in the sensor rings increased the magnitude of the coherence function, particularly in frequency ranges where coherence is already elevated. Increasing the sensor density from 8 (maroon) to 16 (purple) or 32 (red) sensors per ring provides some limited improvement in the convergence of the coherence function to the function developed based on continuous circumferential integration (black).

The third component affecting the magnitude of BFF unsteadiness is the number of sensors per ring. To isolate the impact of sensor azimuthal density, force-per-length BFFs were developed with and without azimuthal coherence factors – longitudinal coherence factors are not applied to force-per-length BFFs. Force-per-length BFFs were developed using 4, 8, 16, and 32 vPTs per ring and compared to the continuously-integrated force-per-length loads developed using uPSP measurements at the same locations as the rings of vPTs. The trends in ΔF_{rms} levels for a sample case are presented in Figure 16.

Trends in rms levels for force-per-length BFFs without azimuthal coherence are presented in Figure 16a. Low azimuthal sensor density resulted in overpredictions in rms levels, since the integration process assumed full coherence across the integration arc length. Increasing the azimuthal sensor density converges the rms levels to the continuous integration BFFs from above – implying overprediction in the overall fluctuation levels, if azimuthal coherence is not applied.

The inclusion of azimuthal coherence factors (Figure 16b) significantly changes the above trends. For most of the stations examined, the inclusion of azimuthal coherence factors resulted in the 4-sensor-based BFFs underpredicting the overall fluctuation level. Increasing the sensor density increased the rms values closer to the continuous integration rms values. 32-sensor ring force-per-length BFFs overpredicted the overall fluctuation. The crossover point from the rms levels being lower than the continuous integration force-per-length BFF rms levels occurred between 8 and 16 sensors in a ring. This finding indicates that the current approach of determining azimuthal coherence factors for reducing overprediction inherent in the azimuthal integration of discrete pressure measurement needs to be refined.
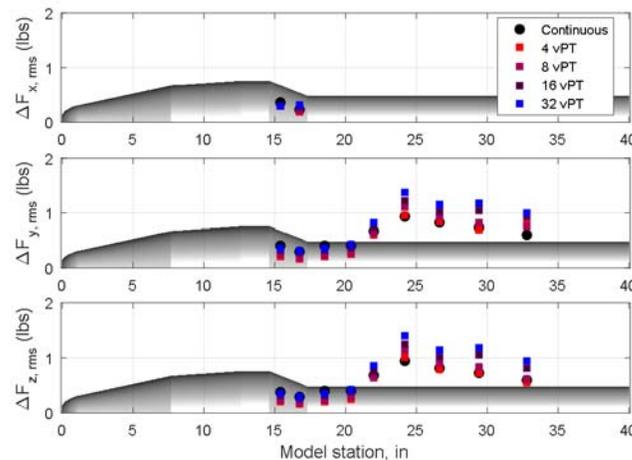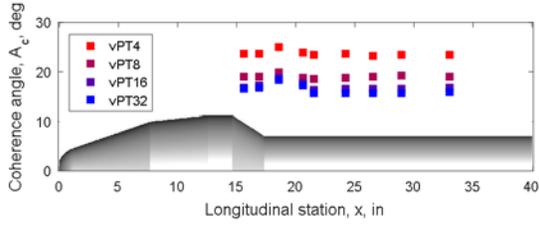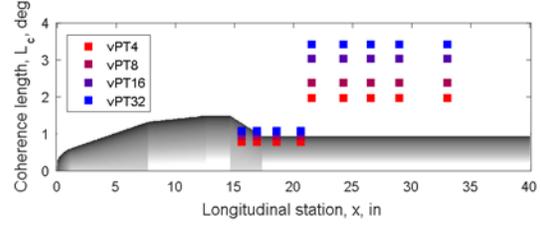

Figure 10. Comparison of BFF ΔF_{rms} continuous vs. discrete, M=0.92, α=0°.
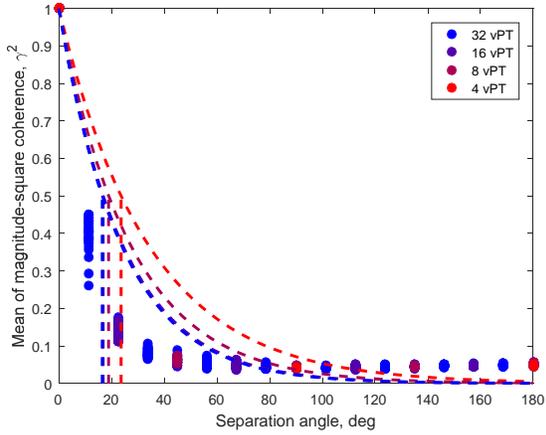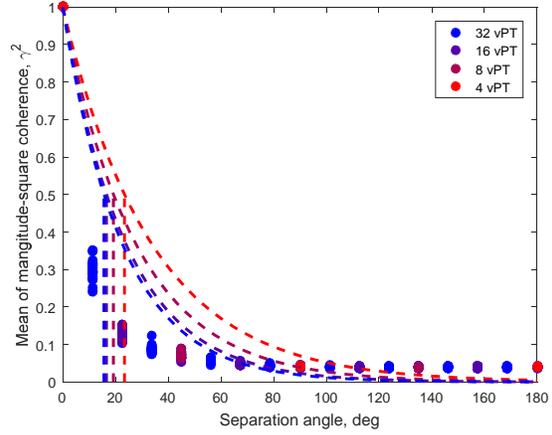
(a) Coherence angles (b) Coherence lengths

Figure 11. Comparison of coherence lengths and angles as a function of sensor circumferential density, M=0.92, α=0°.
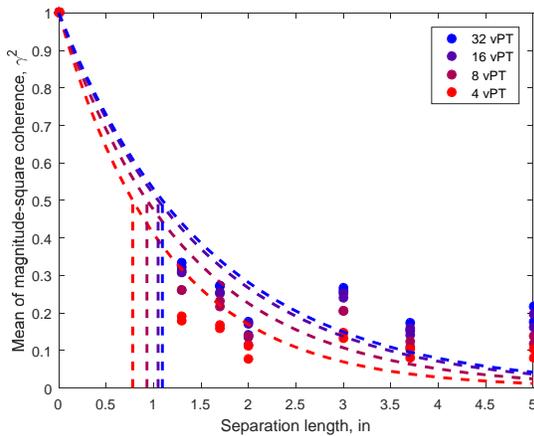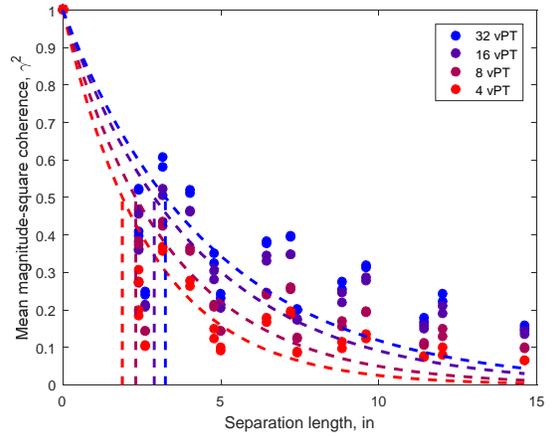

(a) Station x=15.57 in (SF region) (b) Station x=28.97 in (RF region)

Figure 12. Effect of sensor circumferential density on exponential fit of azimuthal coherence decay, M=0.92, α=0°.

(a) SF region (b) RF region

Figure 13. Effect of sensor circumferential density on exponential fit of longitudinal coherence decay, M=0.92, α=0°.
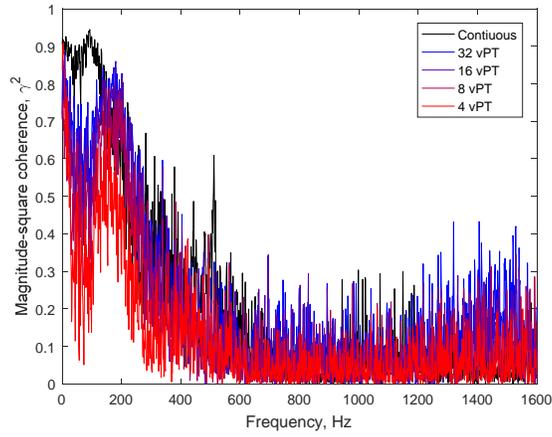
11

Figure 14. Effect of sensor circumferential density on longitudinal coherence in force-per-length F_z between x=15.57 in & x=16.87 in (SF region), M=0.92, α=0°.
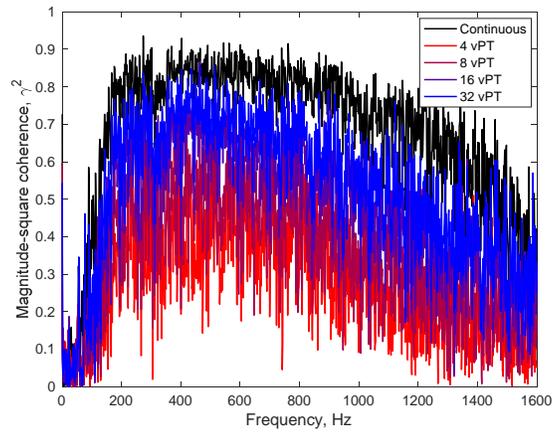

Figure 15. Effect of circumferential sensor density on longitudinal coherence in force-per-length F_z between x=28.97 in & x =33.00 in (RF region), M=0.92, α=0°.

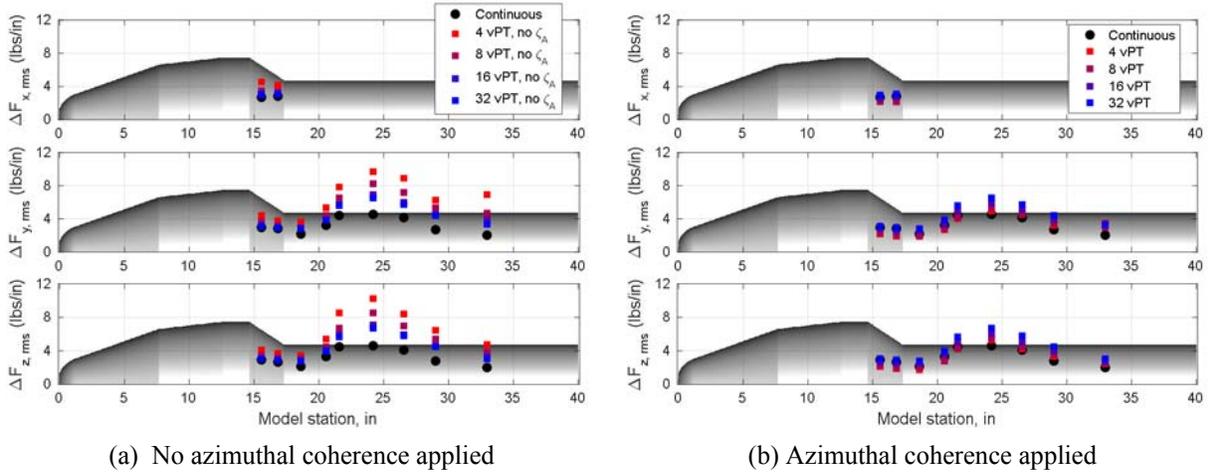(a) No azimuthal coherence applied   (b) Azimuthal coherence applied

Figure 16. Effect of sensor circumferential density on force-per-length BFF unsteadiness, M=0.92, α=0°.

12

3. Spectral Content

Up to this point, the adequacy of the BFF development process has been assessed using rms values of the BFF time histories. From a numerical perspective, root-mean-square of a signal is related to the area under the curve of a power spectral density function (PSD) of the signal in question, thereby providing a simple method to quantify the overall fluctuation in the signal. While this approach lends itself to examining large data sets, it provides no insight into the frequency content of the BFFs – an important consideration when applying BFFs to structural models of a launch vehicle. Missing or additional frequency content in a BFF can result in under- or over-exciting a structural mode in the vehicle structural analysis. The vehicle and component structural design is affected by response considerations and a lack of understanding of the BFF frequency content requires larger uncertainty factors, resulting in a heavier, less efficient structure and ultimately reduced payload capability.

One method to understand the differences in the frequency content of discrete measurement-based BFFs and uPSP-based BFFs is to compare their PSDs. With hundreds of PSDs in this data set, individual PSD comparisons are not a practical approach. Therefore, two-dimensional histograms were developed that provide the distribution of the percent error between PSDs of discrete measurement-based BFFs and uPSP-based BFFs as a function of frequency. The percent error is defined such that a positive value indicates an overprediction. A series of these histograms is presented in Figures 17 through 20. These histograms were developed using the following procedure:

1. PSDs were calculated for BFFs developed using discrete measurements (vPTs) and continuous uPSP integration over the area associated with each ring of sensors for all test conditions.

2. A percent error as a function of frequency is calculated for each corresponding PSD pair.

3. Using all test conditions, a histogram of the error distribution is developed for each PSD frequency bin.

4. A contour plot is assembled based on the histograms calculated in step 3, where the abscissa represents the frequency bins, ordinate represents the percent error, and the color intensity represents the percentage of instances (i.e. probability) within each error bin.

5. The median of this error distribution as a function of frequency represented by a red curve is added. Additionally, green lines envelope 50 percent of all instances about the median value as a function of frequency, while the yellow lines envelop 75 percent of all instances.

The histograms presented in Figures 17 through 20 present the distribution of PSD error for BFFs based on 4, 8, 16, or 32 sensors per ring, respectively. Each figure includes two histograms: the BFFs from the SF Region (subfigure *a*), and second is for BFFs from the RF Region (subfigure *b*). There are three trends to note in these figures. The first observation is that as the number of sensors per ring is increased, the PSDs of discrete measurement-based BFFs shift in the positive (overpredicting) direction. This observation confirms the trend identified through the rms analysis (Figures 6 through 9 and Table 2).

The second observation is that the scatter in the PSD error is larger above the median value (red line) than below it (see the 50 and 75% envelope lines). The other discernable trend is that the skewing in the error distribution is more pronounced at higher frequencies. The most likely cause of this trend is that at higher frequencies the PSD values are smaller, thereby small changes in the PSD magnitude can produce large percent error.

The last observation is that the level of overprediction of the BFFs increases at higher frequencies. These observations hold true for both the SF and RF regions. The 4-sensors per ring BFFs significantly underpredict the BFF fluctuations at low frequencies and overpredict them at high frequencies, although the SF region low-frequency underpredictions are larger than those in the RF region and RF region high-frequency overpredictions are larger than those for the SF region, compare Figures 17(a and b). As the number of sensors per ring increases to 16, the median error of the low-frequency PSD in the RF region is always positive, indicating that in all PSD frequency bins, the discrete measurement-based BFFs are overpredicted at least 50 percent of the time. Increasing the number of sensors per ring to 32 continues the above trends, providing some low-frequency improvements in the SF region, while increasing the overprediction elsewhere.

The underprediction of low frequency signals and overprediction of high frequency signals may be an artifact of the method used to calculate the coherence factors in the development of the BFFs. Coherence factors are calculated using an average of the coherence function over a frequency range. Generally, coherence is highest at low frequencies and attenuates with increasing frequency, therefore, the average coherence value will be lower than the actual low frequency coherence, and greater than the high frequency coherence, as demonstrated in Figure 21. The coherence

factors adjust the effective integration area for the measured pressures, therefore, using an average value in calculating the coherence factors has two unintended consequences: the low frequency pressure signal is integrated over an undersized effective area, and higher frequency signals are integrated over an oversized area. Simply put, at frequencies approaching 1600 Hz, coherence is very low, but the effective integration area is still based on low-frequency coherence, resulting in large overpredictions of the high-frequency PSDs.

The use of average coherence helps explain why the two aerodynamic regions are affected differently by the change in the number of sensors per ring. Figures 14 and 15 present the coherence functions between two force-per-length BFFs in the SF and RF regions, respectively. The sample coherence function from the SF Region is high at low frequencies and quickly drops off – the scenario discussed in the preceding paragraph. The coherence function from the RF region increases at higher frequencies, thereby the mean coherence will be overpredicted at low frequencies as well as high frequencies (above 1200 Hz).

These observations indicate that a frequency-dependent coherence factor formulation should be implemented to more appropriately account for the differences in coherence lengths at various frequencies. A potential approach to accomplish this task is proposed in Reference 13.
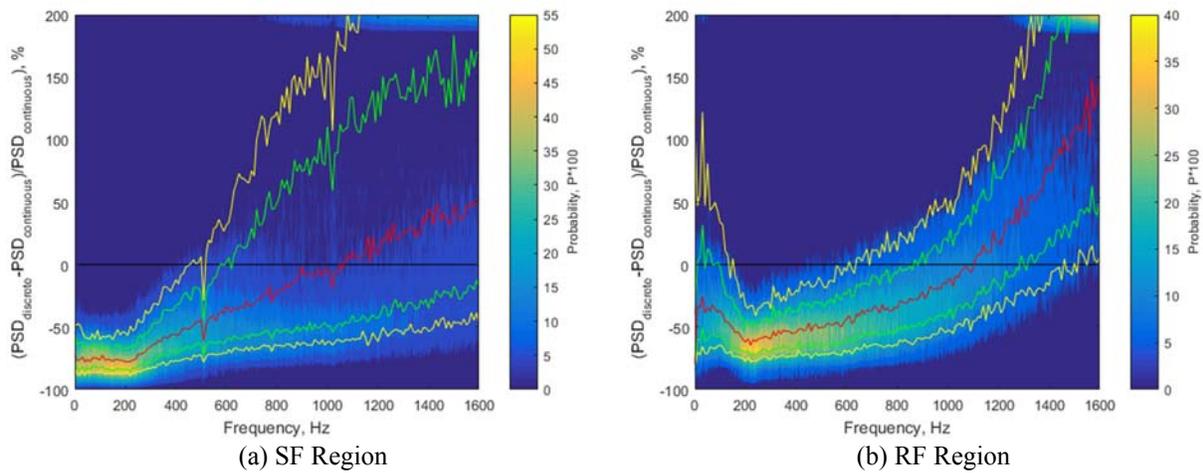

(a) SF Region   (b) RF Region

Figure 17. Histogram of percent difference in BFF PSDs based on continuous integration and 4 vPTs/ring.
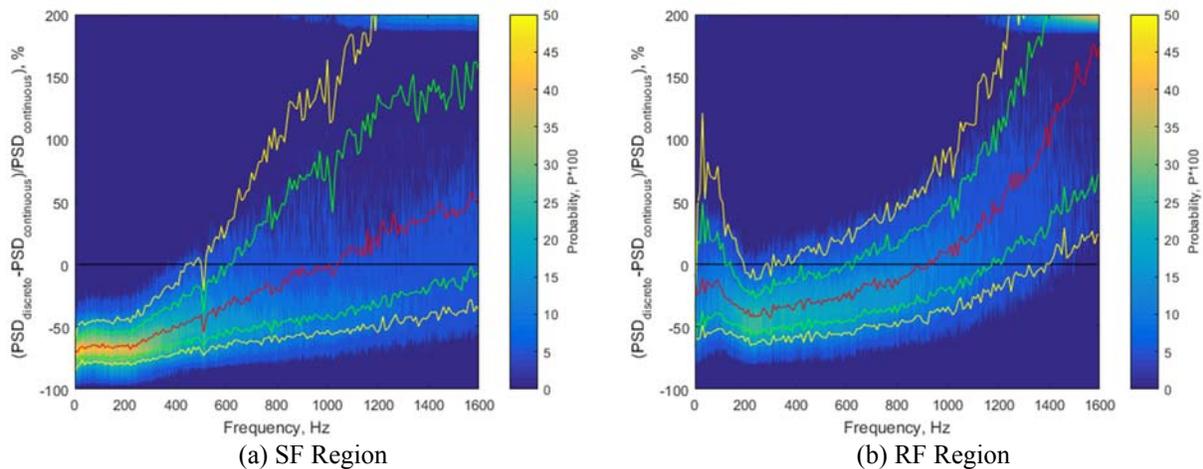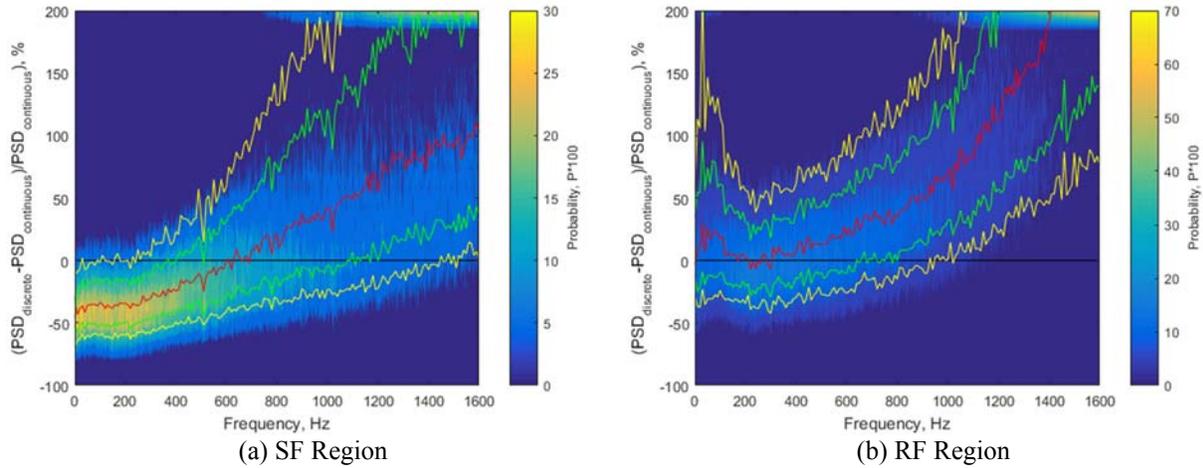

(a) SF Region   (b) RF Region

Figure 18. Histogram of percent difference in BFF PSDs based on continuous integration and 8 vPTs/ring.

14

(a) SF Region　　　　　　　　　　　　　　　(b) RF Region

Figure 19. Histogram of percent difference in BFF PSDs based on continuous integration and 16 vPTs/ring.

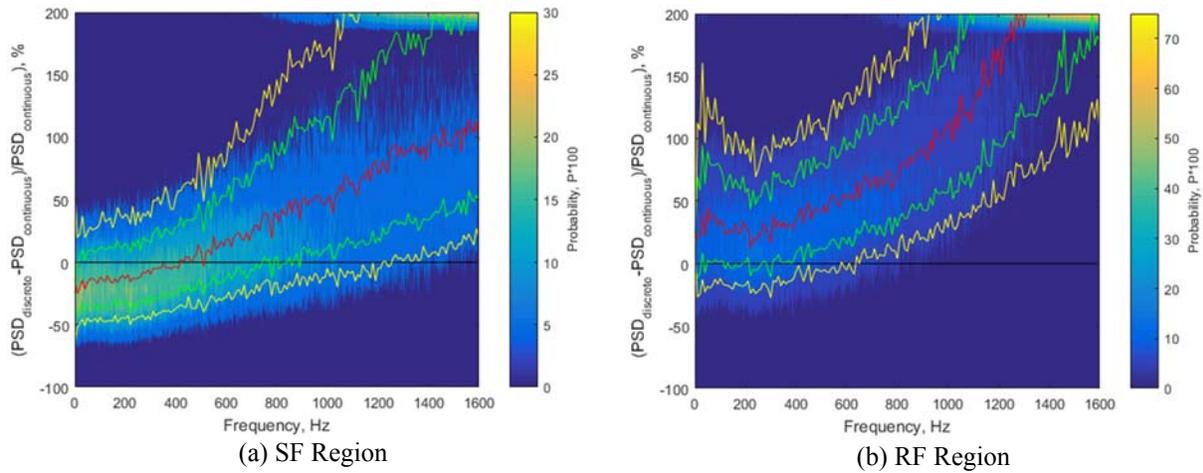(a) SF Region　　　　　　　　　　　　　　　(b) RF Region

Figure 20. Histogram of percent difference in BFF PSDs based on continuous integration and 32 vPTs/ring.
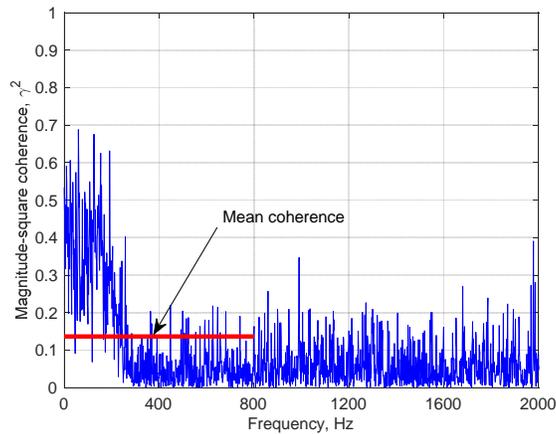

Figure 21. Sample coherence function and mean coherence for frequency range 3 to 800 Hz.

4. Phase Difference

Great care is taken in acquiring time-correlated pressure data during a buffet wind tunnel test, but it was previously unknown how BFF development affects the time correlation of the BFFs. Since the same uPSP data are used to

15

develop both the discrete measurement-based BFFs and the continuous integration BFFs, it is therefore possible to employ cross-PSD analysis to calculate the phase between corresponding BFFs in each data set. The results of this analysis are provided in a series of 2-dimensional histograms presented in Figures 22 through 25. The histograms are created using the same method that is used to create the PSD error histograms (Figures 17 through 20). In these phase histogram plots, positive phase values indicate phase lag of a discrete measurement-based BFF with respect to a continuous uPSP integration BFF.

The histograms in Figures 22 through 25 present the change in phase of BFFs based on 4, 8, 16, and 32 sensors per ring, respectively, relative to a continuous uPSP integration BFF. The median value of the distribution of the phase difference is generally close to 0 degrees, indicating that the current approach to developing BFFs does not introduce a phase shift into the BFFs, statistically speaking. These histograms also indicate that the scatter in the distribution of the phase change increases as a function of frequency. Another notable trend is that increasing the number of sensors per ring reduces the scatter in the distribution of the phase change. Therefore, more sensors per ring tends to reduce the phase error in the BFFs.

Ultimately, the importance of the BFF phase should be determined by applying BFFs with varying amounts of phase shift to the structural model of a vehicle. Changing the phase may affect the response of a vehicle mode, and a Monte Carlo-type analysis of the phase change could provide a measure of sensitivity of the vehicle response to the uncertainty in the BFF phase.
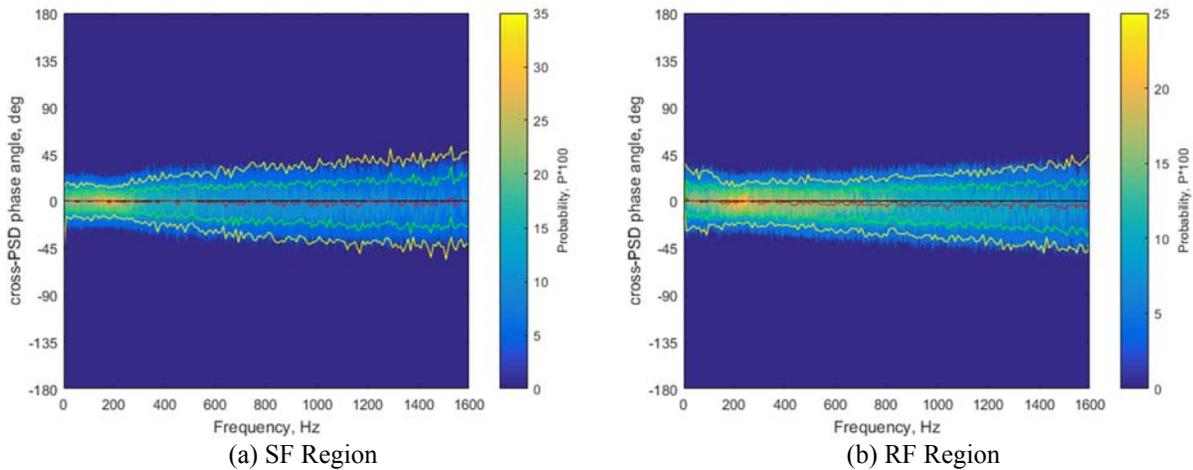

(a) SF Region　　　　　　　　　　　　　　　(b) RF Region

Figure 22. Histogram of phase of BFF CPSD(continuous, 4 vPTs/ring).

(a) SF Region　　　　　　　　　　　　　　　(b) RF Region
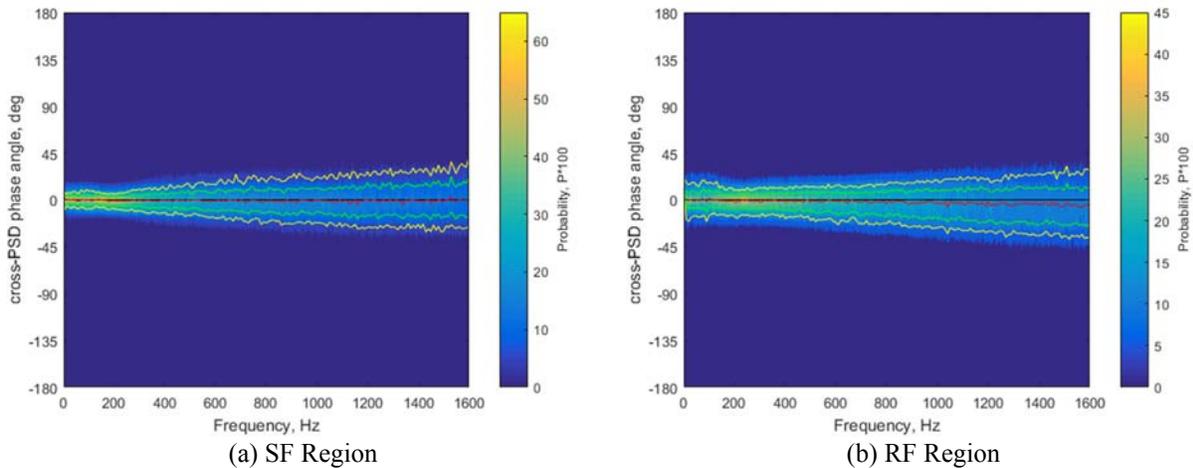
Figure 23. Histogram of phase of BFF CPSD(continuous, 8 vPTs/ring).

16

(a) SF Region   (b) RF Region
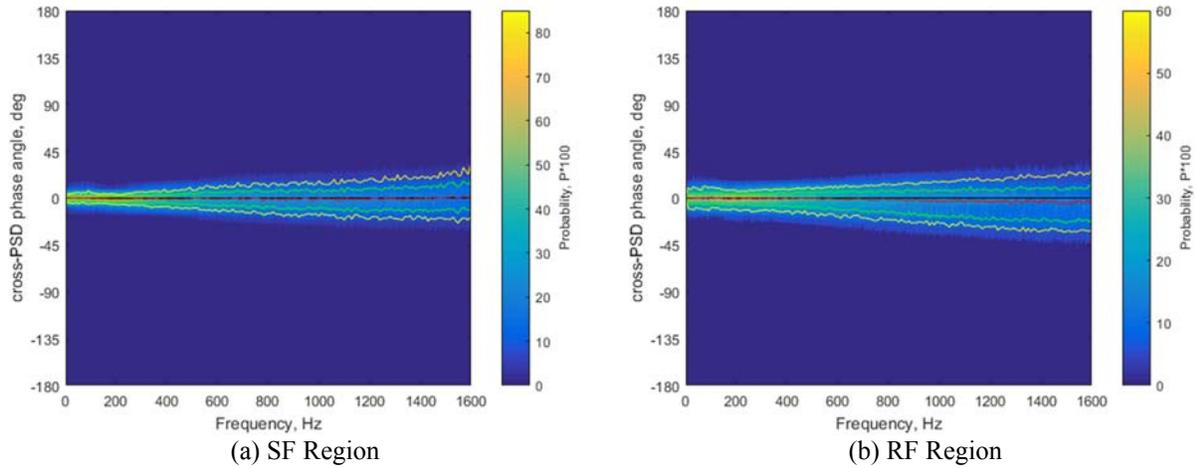
Figure 24. Histogram of phase of BFF CPSD(continuous, 16 vPTs/ring).
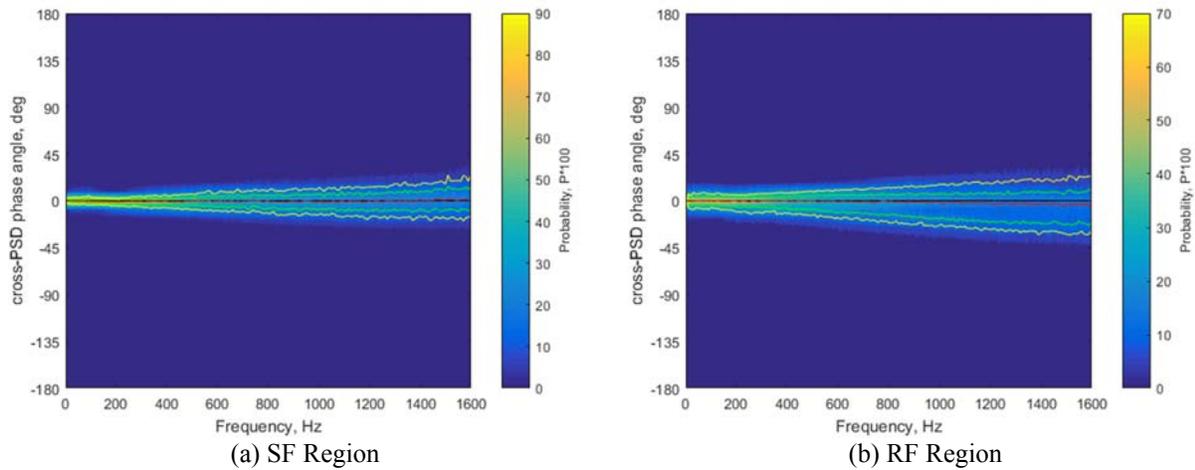

(a) SF Region   (b) RF Region

Figure 25. Histogram of phase of BFF CPSD(continuous, 32 vPTs/ring).

D. Effect of Longitudinal Sensor Ring Density

In the preceding discussion, Section III.A, the section of the BVT model where the uPSP measurements were validated was divided into nine longitudinal segments and BFFs were developed for each segment. To examine the impact of longitudinal sensor density on the resulting BFFs, each of these nine segments was subdivided into a series of longitudinal segments approximately 0.25 inches in length. This division process resulted in 92 segments and a ring of eight axisymmetrically-spaced vPTs was located at the longitudinal center of each new segment. Figure 26 presents the new longitudinal integration boundary distribution. The locations of the longitudinal boundaries of the original nine segments are shown in green and the additional boundaries of the new segments are presented in blue.

The new sensor locations and integration boundaries were used to develop new BFFs using the standard approach outlined in Ref. 7. The 0.25 inch longitudinal integration length for these new BFFs was an order of magnitude shorter than the calculated coherence lengths for all cases – effectively eliminating the longitudinal coherence factor from the BFF calculation. For ease of comparison, the previously-defined aerodynamic regions were not adjusted, even though the increased longitudinal sensor density may better identify the transition station between the SF and RF regions.

The BFFs for the new, smaller segments were grouped together based on the longitudinal integration boundaries of the original BFFs. By summing each of these nine groups of BFFs, composite BFFs equivalent to the original, larger-integration-area BFFs were developed. These composite BFFs can be compared to the original BFF to determine the appropriateness of the longitudinal coherence factors implementation.

17

The rms error between the composite BFFs and the continuous integration BFFs are provided in Figure 27. Comparing the composite BFF rms errors to the original BFFs rms errors in Figure 7, indicates that the shorter longitudinal integration lengths eliminated the mean offset in rms error between the SF and RF regions – the histogram of all the test cases (Figure 27c) exhibits a single peak, Gaussian distribution instead of the dual peak distribution found in Figure 7c. This single peak appears to be located in between the original SF and RF peaks found in Figure 7, indicating that decreasing the longitudinal integration length reduced the underprediction of the SF region BFFs, but increased the underprediction of the RF region BFFs. For completeness, the statistical values for the histogram in Figure 27c are provided in Table 3.

The reason for the collapse of the two peaks in Figure 7c into a single peak in Figure 27c can be inferred by examining the 2-dimensional histograms of the error between PSDs of the combined BFFs and the continuous integration BFFs, provided in Figure 28. Both the SF and RF region 2-dimenstional histograms indicate that the composite BFFs generally underpredict the unsteadiness throughout the entire frequency range of interest. This trend differs from the original BFFs, provided in Figure 18, where the PSDs overpredict the high frequency fluctuations. The shorter longitudinal integration lengths had two other consequences. First, the median value (red line) of the RF region BFFs seem to be more underpredicted in the 400 to 1200 Hz range than the SF region BFFs (compare Figure 28a to Figure 28b), while in the original BFFs (Figure 18), the trend in median values is similar. This difference may contribute to the increase of RF BFF underprediction. The last notable observation is that the shorter integrations lengths reduced the scatter in the histograms compared to the original BFFs (compare range of the 50% (green) and 75% (yellow) envelope lines in Figures 18 and 28).

The difference in the higher-frequency portions of the PSDs may be caused by either the BFF summation process or the short longitudinal integration lengths. Summing the forcing functions calculated at multiple longitudinal stations to produce a combined BFF is the equivalent of producing a BFF by integrating a very coarse uPSP grid – indicating the effect of uPSP surface grid density not the effect of longitudinal sensor spacing on BFFs. On the other hand, the shortened longitudinal integration lengths of the 92 segments eliminated the longitudinal coherence factors. The change in the PSDs for the combined BFFs may be an indication that the present implementation of the longitudinal coherence factors is not appropriate for adjusting the high frequency content of BFF. To properly ascertain this issue, new continuous integration BFFs need to be developed for the smaller integration areas and compared to the small-segment BFFs.
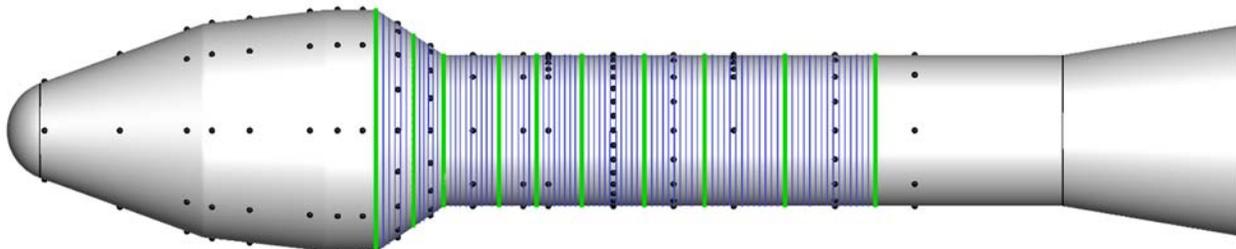

Figure 26. Longitudinal integration boundaries for increased longitudinal sensor density.
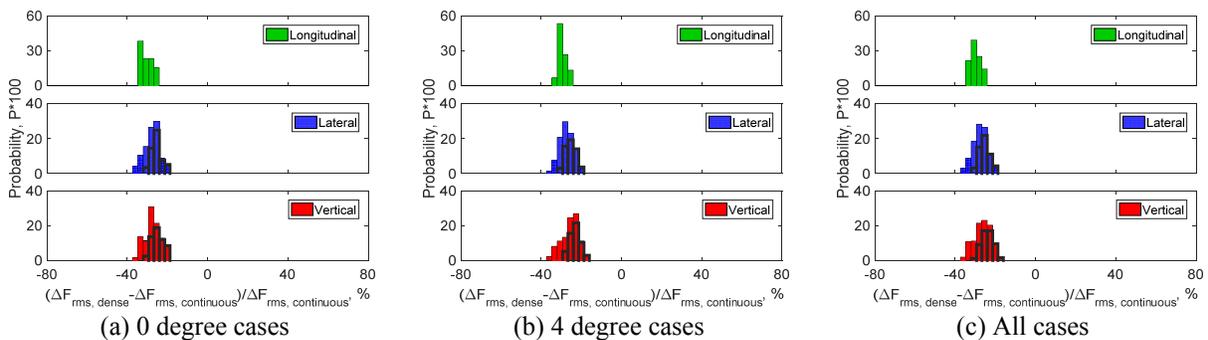

(a) 0 degree cases   (b) 4 degree cases   (c) All cases

Figure 27. Histogram of percent error in BFF ΔF_{rms} based on continuous integration and combined BFFs, 8 vPTs/ring, (RF region data defined by thicker outline) .

18

Table 3. Statistical values of percent error in BFF ΔF_{rms} based on continuous integration and combined BFFs, 8 vPTs/ring.

		Long.	Lateral	Vertical
Mean	SF Region	-29.8	-30.2	-29.5
	RF Region	n/a	-25.4	-23.9
	Both Regions	-29.8	-27.6	-26.4
Median	SF Region	-30.2	-30.2	-29.6
	RF Region	n/a	-25.6	-23.9
	Both Regions	-30.2	-27.3	-26.4
Standard deviation	SF Region	2.5	2.9	3.5
	RF Region	n/a	2.5	2.8
	Both Regions	2.5	3.6	4.2
% under-prediction	SF Region	100	100	100
	RF Region	n/a	100	100
	Both Regions	100	100	100

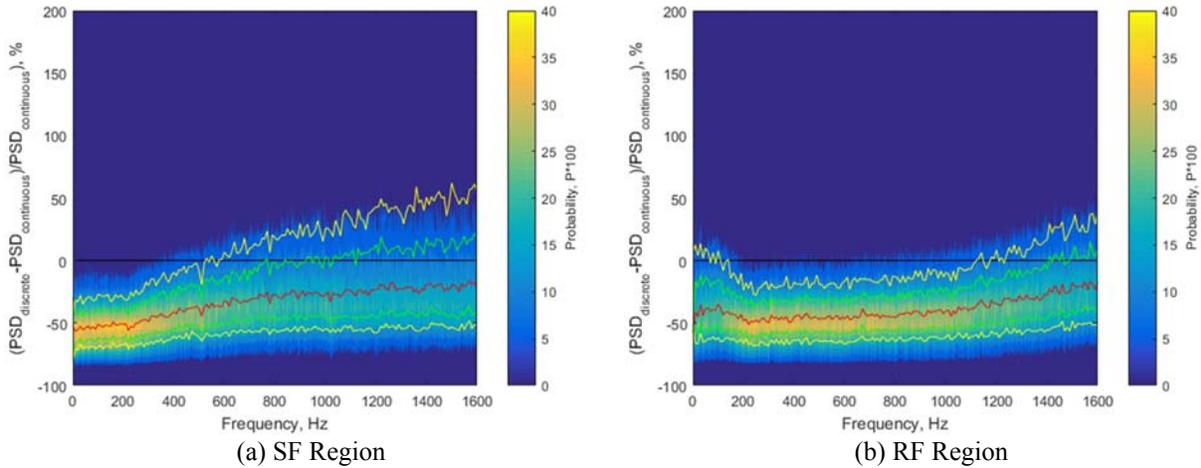(a) SF Region (b) RF Region

Figure 28. Histogram of percent error in BFF PSDs based on continuous integration and combined BFFs, 8 vPTs/ring.

E. Effect of Longitudinal Placement of Sensor Ring within Each Integration Region

One of the assumptions in the BFF development process is that, unless there is a large OML change, the surface area integration boundaries associated with each transducer are set to be the midpoints between adjacent transducers. While this assumption is intuitive in nature, and the phase change histograms (Figures 22 through 25) indicate that this is the correct approach to defining the integration boundaries, the sensitivity of discrete measurement-based BFFs to the longitudinal location of sensors within the integration region was examined to provide further confirmation of this assumption. To conduct this study, the longitudinal integration boundaries for the rings of sensors were held constant, and new rings of vPT were extracted from the uPSP data near the forward and aft ends of the integrations segments. For this study, only the BFFs based on 8 vPTs per ring were examined.

These new vPTs were used to develop BFFs for the same integration areas, and PSD error and cross PSD phase 2-dimensional histograms were created and are presented in Figures 29 through 32. The change in longitudinal location of the sensors within the integration boundaries had a minor effect on the magnitude of the PSD error, compare Figures 29 and 30 to Figure 18, although this observation may not hold true for large integration areas with significantly varying pressure gradients.

Conversely, the longitudinal location of the sensors within each integration area significantly affects the phase of the discrete-measurement-based BFF relative to the continuous integration BFF. Figures 31 and 32 present 2-dimensional histograms demonstrating the effect of longitudinal sensor placement on the phase angle difference between discrete-

19

measurement-based and continuous integration BFFs. In Figure 31, the case where the sensors are located towards the forward end of the integration segments, the histogram indicates that moving the sensors forward in the integration area introduced a negative phase angle bias in the histogram, particularly at higher frequencies, indicating a phase lead in the discrete measurement based BFFs relative to the continuous integration BFFs (compare Figure 31 to Figure 23). The opposite trend in phase is noted when the sensors are located towards the aft end of the integration segment, Figure 32. These observations suggest that sensors should be located close to the center of each integration region.

It should be noted that in both cases, the phase difference in the RF region seems more sensitive to the longitudinal placement of sensors (compare subfigure *a* to subfigure *b* in Figures 31 and 32). The cause of this difference is that the integration areas in the RF regions are larger (see Figure 26), so the longitudinal distance that the sensors were moved relative to their original placement was also larger, resulting in a greater change in the phase of the BFFs.

The discussion in the section was limited to BFFs based on 8 vPTs per ring. The same analysis was conducted for BFFs based on 4 vPTs per ring (not presented) and it was found that the trends noted above did not differ substantially, an indication that azimuthal sensor density does not affect the above conclusions.
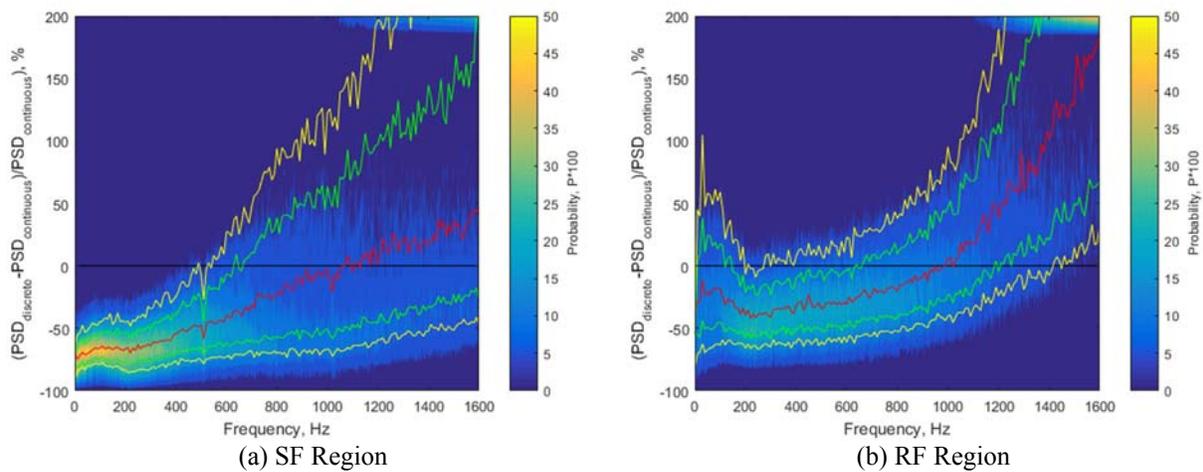

(a) SF Region	(b) RF Region

Figure 29. Histogram of percent error in BFF PSDs based on continuous integration and 8 vPTs/ring, forward sensor location.
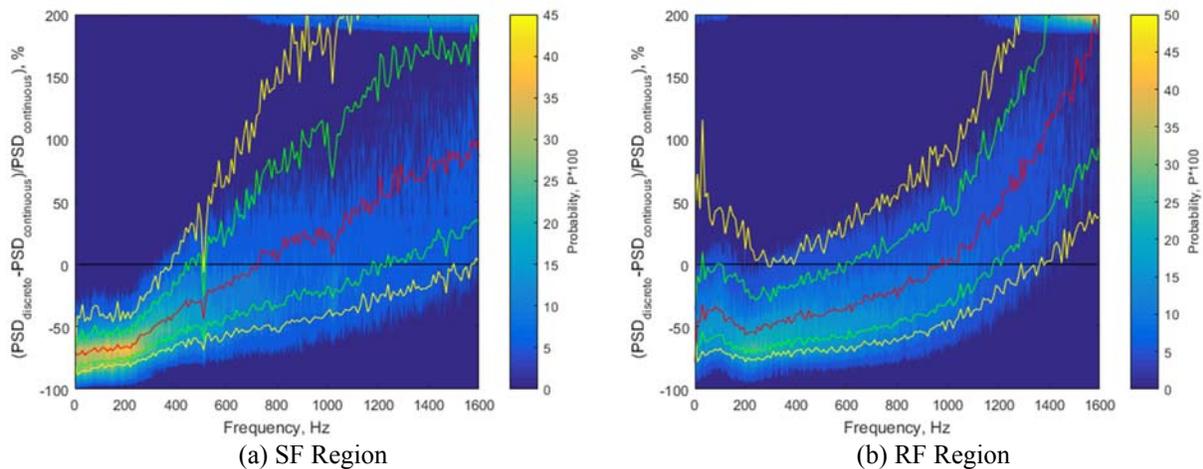

(a) SF Region	(b) RF Region

Figure 30. Histogram of percent error in BFF PSDs based on continuous integration and 8 vPTs/ring, aft sensor location.

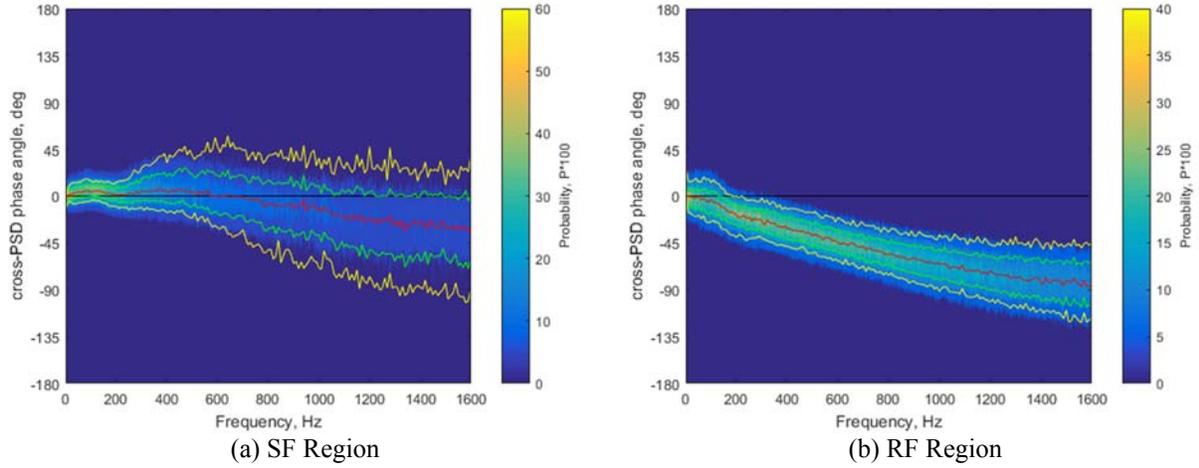(a) SF Region   (b) RF Region

Figure 31. Histogram of phase of BFF CPSD(continuous, 8 vPTs/ring), forward sensor location.

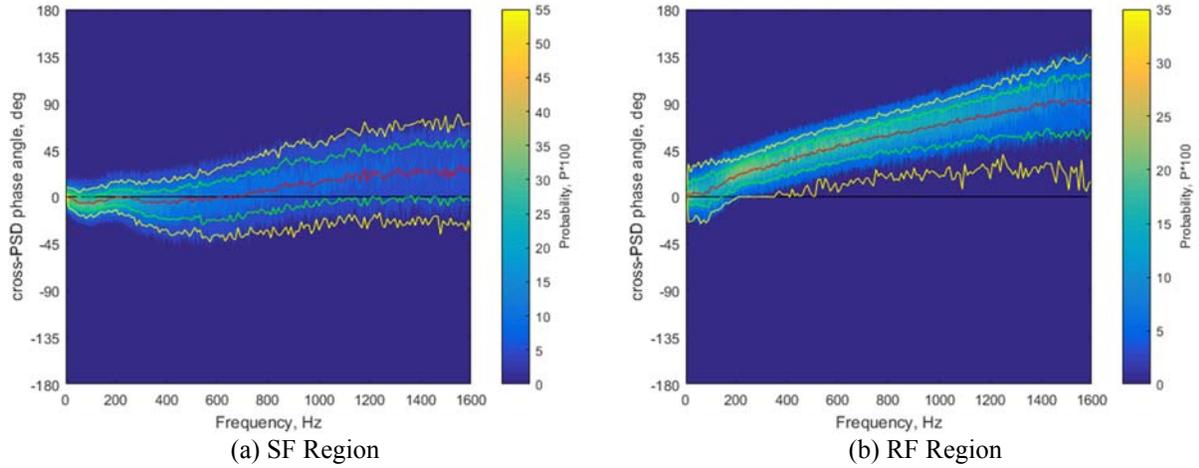(a) SF Region   (b) RF Region

Figure 32. Histogram of phase of BFF CPSD(continuous, 8 vPTs/ring), aft sensor location.

F. Center of Pressure

The BFFs for each longitudinal segment of the launch vehicle are based on a single ring of sensors measuring pressure at that particular station within the segment. A single ring of sensors cannot provide an accurate estimate of the location center of pressure for a given segment due to the spatially- and temporally-varying nature of the surface pressure. The BFF development process assumes that the measured pressure from each sensor is constant over its area of integration and therefore the center of pressure for each integration segment is the centroid of the projected area.

The appropriateness of this center of pressure location approximation cannot be ascertained using sparsely-spaced discrete pressure measurements, but the uPSP data provides the ability to do so. To accomplish this task, moments about the vehicle nose are calculated by integrating uPSP surface pressure for each longitudinal segment of the model and dividing by the net force produced by the pressure on the same longitudinal segment – see equation below,

$$\tilde{x}_{cp}(t) = \frac{\iint P(x,\theta,t)\hat{u}(x,\theta)r(x)xd\theta dx}{\iint P(x,\theta,t)\hat{u}(x,\theta)r(x)d\theta dx}$$

where $\tilde{x}_{cp}(t)$ is the time history of the center of pressure in the lateral and vertical directions, P is the surface pressure, $\hat{u}$ is the unit surface normal vector, θ is the azimuth angle, r is the radius, and x is the longitudinal coordinate.

21

The histograms of center of pressure time histories for each integration segment, presented in Figure 33, were created utilizing data from all 28 uPSP cases available for this study with the longitudinal center of pressure location for each model segment normalized by the longitudinal length of the segment. The leading edge of the segment is located at 0 and trailing edge of the segment is located at a value of 100. Each histogram includes the normalized mean value for the center of pressure location and the normalized standard variation of the center of pressure motion. The vertical red line represents the center of pressure location assumed by the BFF development analysis, which is based on the geometry of the model segment.

The histograms in Figure 33 indicate that assuming that the center of pressure is located at the centroid of the projected area is a reasonable one. For all BFFs, the assumed center of pressure was within three percent of the average location of the actual center of pressure. The standard deviation of the center of pressure is smaller on the frustum, Figures 33(a through d), than on the barrel section of the model, Figures 33(e through r). This difference in standard deviation implies that the motion of the center of pressure is much more dynamic on the barrel section of the model than on the frustum.
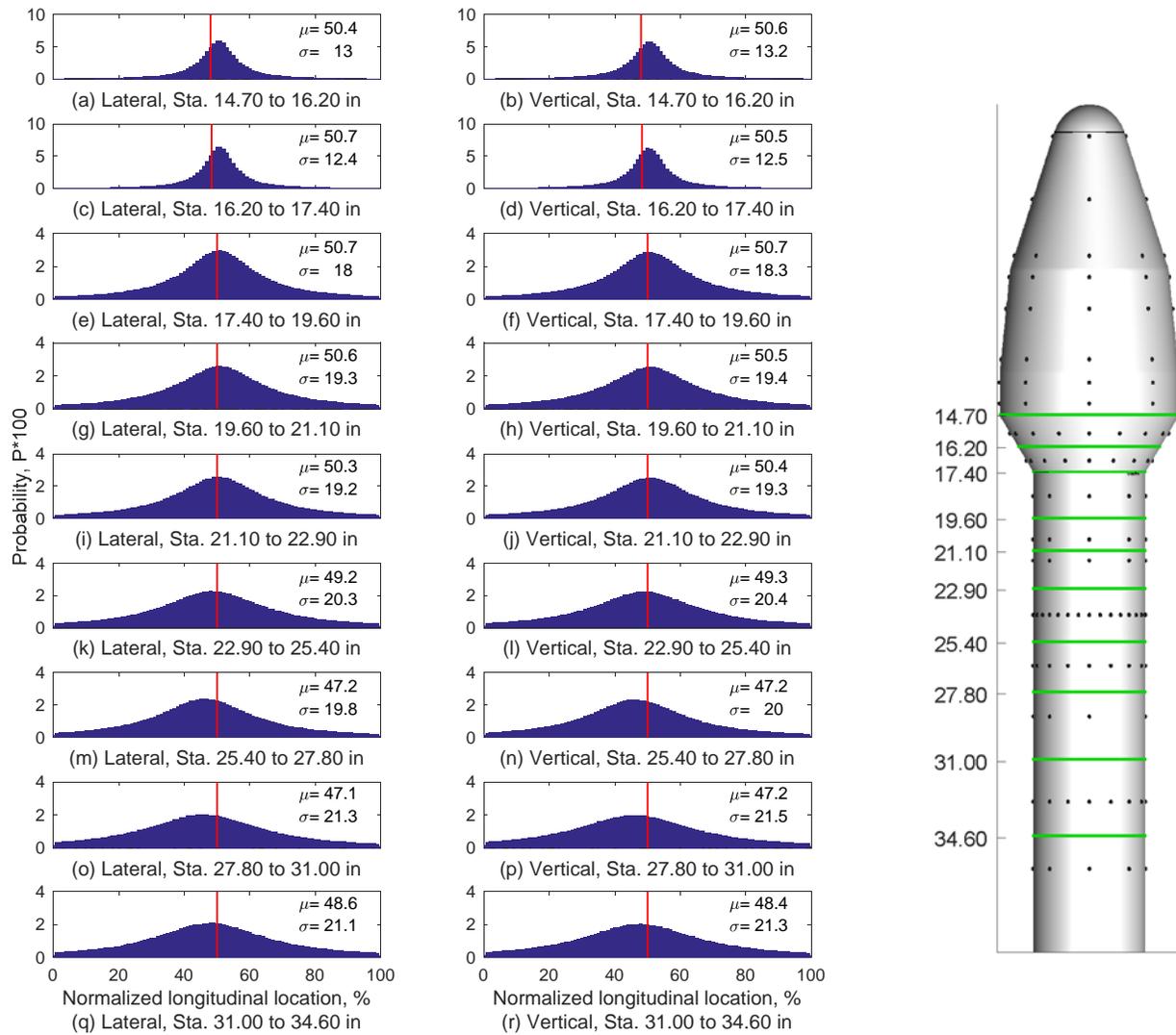

Figure 33. Histogram of the variation in the vertical and lateral center of pressure location.

22

IV.   Conclusions

A wind tunnel test of a generic launch vehicle forebody was conducted at the Ames Unitary Plan Wind Tunnel to characterize its transonic buffet environment. The test used a highly instrumented version of the Coe and Nute Model 11 test article first examined in the 1960s. The primary measurement technique used during this test was unsteady pressure sensitive paint (uPSP). This optical measurement technique provided unsteady pressure measurements at over 300,000 locations on the surface of the model – a continuous measurement of the surface pressures compared to the traditional, sparsely-spaced discrete pressure measurements. This high spatial surface density measurement technique provided an opportunity to examine in depth the assumptions underpinning the development of buffet forcing functions (BFFs), used in the development of the Space Launch System (SLS) vehicle. This task was accomplished by extracting pressure measurements at discrete locations on the model (typical for a standard launch vehicle buffet test) from the uPSP dataset, developing BFFs using the analytical techniques used by the SLS program, and comparing them to equivalent forces developed by continuously integrating the uPSP data.

Comparison of discrete measurement-based BFFs to continuous uPSP-based BFFs indicates that

- Utilizing a pressure sensor distribution typical for a launch vehicle buffet model resulted in significant under-predictions in the overall BFF fluctuations, based on root-mean-square (mean removed) calculation. Power spectral density functions indicated that the BFFs underpredicted the low frequency content, while over-predicting the high frequency content in the BFFs. These trends may be caused by the implementation of the coherence factors based on the mean value of the coherence function over a selected frequency range. This approach underestimates the coherence function at frequencies where its value is large and overestimates the coherence function at frequencies where its value is small.

- The approach to locating the integration boundaries at major changes in the model outer mold line and halfway points between adjacent sensors does not introduce significant phase shift in the BFFs compared to the continuous integration BFFs.

- The current BFF development process does not introduce large phase shift in the discrete measurement based-BFFs relative to continuously integrated BFFs. The phase shift is reduced with increasing number of sensors in a ring of sensors.

- Overall fluctuation of the BFFs is highly sensitive to the azimuthal sensor density. Without azimuthal coherence factors, the overall fluctuation of the BFFs is overestimated and decreases with increasing sensor density. Applying azimuthal coherence factors results in underestimation of the overall fluctuation when the BFFs are based on four axisymmetrically distributed sensors, and generally overestimated when 16 or more sensors are used.

- Longitudinal sensor density variation indicates that the large overprediction of the higher frequency component of the BFFs may be caused by the long longitudinal integration lengths that are not appropriately adjusted by the coherence factor. These factors are based on a mean value of the coherence function across a specified frequency range. This approach underestimates the coherence function at frequencies where its value is large and overestimates the coherence function at frequencies where its value is small. A frequency-based coherence factor may resolve this estimation problem.

- The center of pressure for various longitudinal segments of the model were calculated using uPSP data. The resulting center of pressure time histories indicate that the motion of the center of pressure is highly dynamic, but the mean value corresponds well with the assumption that the center of pressure acts at the centroid of the projected area of the integration region.

V.   References

1. Cole, H.A. Jr, Erickson, A. L., and Rainey, A. G. "Buffeting during Atmospheric Ascent," NASA SP-8001, May 1964, revised 1970.

2. Ericsson, L. E., "Unsteady Flow Separation can Endanger the Structural Integrity of Aerospace Launch Vehicles," Journal of Spacecraft and Rockets 2001; 38: 168–179.

3. Robinson, R.C., Wilcox, P.R., Gambucci, B. J., et al, "Dynamic Response of a Family of Axisymmetric Hammerhead Models to Unsteady Aerodynamic Loading," NASA TN D-4504, 1968.

4. Alter, S. J., Brauckmann, G. J., Kleb, W. L., Streett, C., Glass, C., Schuster, D. M., "Time-Accurate Unsteady Pressure Loads Simulated for the Space Launch System at Wind Tunnel Conditions," 33rd AIAA Applied Aerodynamics Conference, 2015, AIAA 2015-3149, doi:10.2514/6.2015-3149.

5. Brauckmann, G. J., Streett, C., Kleb, W. L., Alter, S. J., Glass, C., "Computational and Experimental Unsteady Pressures for Alternate SLS Booster Nose Shapes," 53rd AIAA Aerospace Sciences Meeting, Kissimmee, FL, 5-9 Jan 2015, AIAA 2015-0559, 2015, doi: 10.2514/6.2015-0559.

6. Piatak, D. J., Sekula, M. K., Rausch, R., Florance, J. R., and Ivanco, T. G., "Overview of the Space Launch System Transonic Buffet Environment Test Program", 53rd AIAA Aerospace Sciences Meeting, Kissimmee, FL, 5-9 Jan 2015, AIAA 2015-0557, doi: 10.2514/6.2015-0557.

7. Sekula, M.K., Piatak, D.J., Rausch, R.D., "Space Launch System Program (SLSP) Vehicle Aerodynamic Substantiation Report for the SLS-1000X Buffet Forcing Function Database," NASA-TM-2018-21930, May 2018.

8. Schuster, D. M, et al, "Investigation of Unsteady Pressure-Sensitive Paint (uPSP) and a Dynamic Load Balance to Predict Launch Vehicle Buffet Environments," NESC-RP-14-00962, November 2016.

9. Coe, C. F. and Nute, J. B., "Steady and Fluctuation Pressures at Transonic Speeds on Hammerhead Launch Vehicles," NASA TMX-778, 1962.

10. Sekula, M. K., et al, "NASA Test Summary Document for the 3.5 Percent Ares I-X Rigid Buffet Model; Transonic Dynamics Tunnel Test #599 November-December 2007", NASA-TP-2015-218703, March 2015.

11. Sellers, M. E. and Nelson, M. A. "Dynamic Pressure-Sensitive Paint Demonstration in AEDC Propulsion Wind Tunnel 16T." AIAA Paper 2016-1146, 54th AIAA Aerospace Sciences Meeting, San Diego, CA, January 2016.

12. Sellers, M. E. and Nelson, M. A., Roozeboom, N. H. and Burnside, N. J. "Evaluation of Unsteady Pressure Sensitive Paint Measurement Technique for Space Launch Vehicle Buffet Determination." AIAA Paper 2017-1402, 55th AIAA Aerospace Sciences Meeting, Grapevine, TX, January 2017.

13. Panda, J., "Experimental Verification of Buffet Calculations Procedure Using Unsteady Pressure-Sensitive Paint," Journal of Aircraft, Vol.54, No. 5, September-October 2017, doi: 10.2514/1.C033917.